





LETTER TO THE EDITOR

Tidally locked rotation of the dwarf planet (136199) Eris discovered via long-term ground-based and space photometry[★]

R. Szakáts^{1,2} , Cs. Kiss^{1,2,3} , J. L. Ortiz⁶ , N. Morales⁶ , A. Pál^{1,2,4}, T. G. Müller⁵ , J. Greiner⁵ ,
P. Santos-Sanz⁶ , G. Marton¹ , R. Duffard⁶ , P. Sági^{1,2,4} , and E. Forgács-Dajka^{7,8,9,10}

¹ Konkoly Observatory, Research Centre for Astronomy and Earth Sciences, Konkoly Thege 15-17, 1121 Budapest, Hungary

² CSFK, MTA Centre of Excellence, Konkoly Thege Miklós út 15-17, 1121 Budapest, Hungary

e-mail: szakats.robert@csfk.org

³ ELTE Eötvös Loránd University, Institute of Physics, Budapest, Hungary

⁴ Eötvös Loránd University, Pázmány Péter sétány 1/A, 1171 Budapest, Hungary

⁵ Max-Planck-Institut für extraterrestrische Physik, P.O. Box 1312, 85748 Garching, Germany

⁶ Instituto de Astrofísica de Andalucía, IAA-CSIC, Glorieta de la Astronomía s/n, 18008 Granada, Spain

⁷ Department of Astronomy, Institute of Geography and Earth Sciences, Eötvös Loránd University, Pázmány Péter sétány 1/A, 1117 Budapest, Hungary

⁸ Centre for Astrophysics and Space Science, Eötvös Loránd University, Pázmány Péter sétány 1/A, 1117 Budapest, Hungary

⁹ ELKH-SZTE Stellar Astrophysics Research Group, Szegedi út, Kt. 766, 6500 Baja, Hungary

¹⁰ Wigner Research Centre for Physics, PO Box 49, Budapest 1525, Hungary

Received 13 October 2022 / Accepted 14 November 2022

ABSTRACT

The rotational states of the members in the dwarf planet-satellite systems in the trans-Neptunian region are determined by formation conditions and the tidal interaction between the components. These rotational characteristics serve as prime tracers of their evolution. A number of authors have claimed a very broad range of values for the rotation period for the dwarf planet Eris, ranging from a few hours to a rotation that is (nearly) synchronous with the orbital period (15.8 d) of its satellite, Dysnomia. In this Letter, we present new light curve data for Eris, taken with $\sim 1\text{--}2$ m-class ground based telescopes and with the TESS and *Gaia* space telescopes. The TESS data did not provide a well-defined light curve period, but it could be used to constrain light curve variations to a maximum possible light curve amplitude of $\Delta m \leq 0.03$ mag ($1\text{-}\sigma$) for $P \leq 24$ h periods. Both the combined ground-based data and *Gaia* measurements unambiguously point to a light curve period equal to the orbital period of Dysnomia, $P = 15.8$ d, with a light curve amplitude of $\Delta m \approx 0.03$ mag, indicating that the rotation of Eris is tidally locked. Assuming that Dysnomia has a collisional origin, calculations with a simple tidal evolution model show that Dysnomia must be relatively massive (mass ratio of $q = 0.01\text{--}0.03$) and large (radius of $R_s \geq 300$ km) to have the potential to slow Eris down to a synchronised rotation. These simulations also indicate that (assuming tidal parameters usually considered for trans-Neptunian objects) the density of Dysnomia should be $1.8\text{--}2.4$ g cm⁻³. This is an exceptionally high value among similarly sized trans-Neptunian objects, setting important constraints on their formation conditions.

Key words. Kuiper belt objects: individual: (136199) Eris – methods: observational – techniques: photometric

1. Introduction

The largest ($D \gtrsim 1000$ km) Solar System objects, namely, dwarf planets, represent a separate class among trans-Neptunian objects with distinct surface characteristics and internal properties as well as with a high incidence of satellites (Brown et al. 2006; Kiss et al. 2017). The present rotational state of these large bodies are assumed to be a combined outcome of formation conditions and tidal interactions in the case of a massive satellite, therefore their rotational light curves and the derived properties are important clues to unraveling their histories. Among these objects, we have the Pluto–Charon system on the one hand, which is known to be tidally locked (Dobrovolskis et al. 1997), whereas Haumea is an extremely fast rotator with a system of two satellites whereby

the more massive satellite has not reached rotational synchronisation with its orbital period (Hastings et al. 2016). The rotation periods of other trans-Neptunian dwarf planets range from a few hours to a few days (e.g., Quaoar, Gonggong and Make-make; Ortiz et al. 2003; Pál et al. 2016; Hromakina et al. 2019), indicating a wide range of formation conditions and tidal interactions. For these objects with relatively long rotation periods, the light curve is expected to be caused by albedo variegations on the surface instead of being spin-shape driven. Eris is the most massive currently known dwarf planet, with a satellite, Dysnomia (Brown & Schaller 2007). Recently Holler et al. (2021) obtained an updated orbit of Eris' satellite, Dysnomia, with a corrected orbital period of $P_{\text{orb}} = 15.785899 \pm 0.000050$ d. They suggested various possible reasons for the observed non-Keplerian orbit of the satellite, including the precession of Dysnomia's orbit due to the oblateness of Eris, an irregularly shaped Dysnomia, an unseen interior satellite, or center-of-light vs. center-of-body offsets.

[★] Full Tables A.1., A.2., A.4 are only available at the CDS via anonymous ftp to cdsarc.cds.unistra.fr (130.79.128.5) or via <https://cdsarc.cds.unistra.fr/viz-bin/cat/J/A+A/669/L3>

Several light curve studies can be found in the literature providing very different rotation periods. [Lin et al. \(2007\)](#) obtained a light curve period of $3^{\text{h}}55$ with an amplitude of $\Delta m \leq 0^{\text{m}}05$ using a 1 m-class ground based telescope. A low amplitude visual light curve of Eris was tentatively detected by [Roe et al. \(2008\)](#), with a period of $P = 1^{\text{d}}08 \pm 0^{\text{d}}02$, and with a peak-to-valley amplitude upper limit of $\sim 0^{\text{m}}1$ based on Swift satellite data. They also reported that the shape of the light curve is likely not sinusoidal, indicating the presence of a dark patch which is visible in part of the rotation period only. [Duffard et al. \(2008\)](#) obtained a light curve period of $13^{\text{h}}7$ at a high confidence level, also using a 1 m class telescope. [Carraro et al. \(2006\)](#) did not obtain a definite rotation period, just a lower limit of ~ 5 d, and also [Rabinowitz et al. \(2007\)](#) and [Sheppard \(2007\)](#) could not identify any period in their data. [Rabinowitz & Owainati \(2014\)](#) reported on a possible synchronous rotation of the Eris–Dysnomia system, with a dominant periodicity in the light curve matching the orbital period of ~ 15.8 days. [Holler et al. \(2020\)](#) suggested that the rotation of Eris is near-synchronous, with a period of $P = 14.56 \pm 0.01$ d, indicating that the system is not yet fully tidally evolved.

In this Letter, we present the analysis of long-term brightness monitoring data collected from various instruments, including the TESS and *Gaia* space telescopes, along with several ground-based telescopes that cover a wide range of possible periods – from a few hours to a rotation synchronised with the orbital motion of the satellite. Due to its sampling rate and duration, TESS data could be used to investigate periods from a few hours to a few days. Ground-based data were typically measured in blocks covering a few nights, with (very) long gaps between the blocks; this allowed us to search for light curve periods in the range between a few days up to that of a synchronised rotation (15.8 d). The sparse sampling of the *Gaia* data allowed us to search for rotation periods in this latter range as well. These observations and the data reduction are described in detail in [Appendix A.1](#). A summary of the analysis of these data and the description of curve period identification are presented in [Sect. 2](#). Using the currently known characteristics of the system we applied a simple tidal evolution model to try to match the rotation period that we obtained from our light curve measurements ([Sect. 3](#)). Our conclusions are given in [Sect. 4](#).

2. Periods identified across the various data sets

2.1. TESS

The TESS space telescope data can be used to search for possible light curve periods in the range of a few hours to a few days (see [Appendix A.1.1](#)) and we were able to identify a period with a residual minimum at a frequency of $f = 0.411 \pm 0.018$ cycle day⁻¹ (denoted as c d^{-1} , hereafter) which corresponds to a period of $P = 58.394 \pm 2.571$ h, with a light curve amplitude of $\Delta m = 0.132 \pm 0.037$ mag (after correcting for instrumental effects). This frequency, however, is considered to be tentative (1.8σ) due to the significantly increased noise at frequencies below 1 c d^{-1} . At frequencies above 1 c d^{-1} , however, a 1σ upper limit of 0.03 mag amplitude (peak-to-peak) could be obtained, indicating that no light curve period above this amplitude level is present at these shorter periods ($P \leq 24$ h).

2.2. Ground-based data

We used a large set of ground based data ([Appendix A.3](#)), which is partly made up of new measurements using several

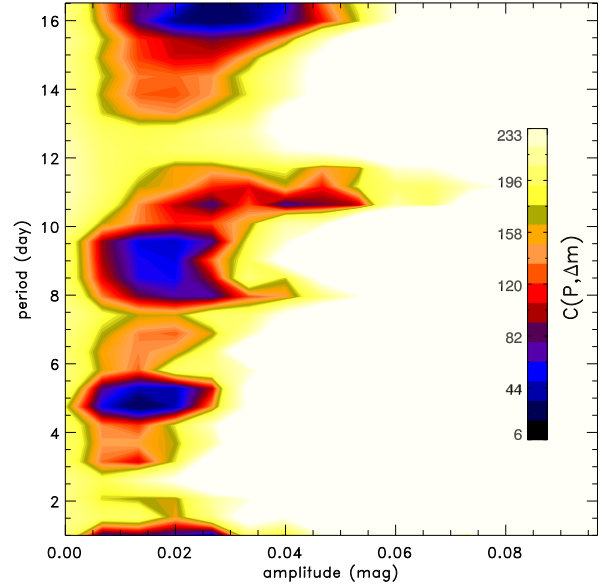


Fig. 1. $C(P, \Delta m)$ contour map; The most prominent minima is identified at a period of ~ 16 d, very close to the orbital period of Dysnomia, 15.78 d (see text for details).

1–2 m-class telescopes (see [Table A.2](#)), supplemented by measurements taken from the literature, including ground-based data from ([Carraro et al. 2006](#); [Rabinowitz et al. 2007](#); [Sheppard 2007](#); [Duffard et al. 2008](#)), and the *Swift* satellite data from [Roe et al. \(2008\)](#). We used a residual minimisation method (see [Appendix A.5](#)) to find the light curve amplitude and period best matched by this large data set. The efficiency of the method was tested using synthetic light curves, using a sampling similar to the real Eris data. We assumed that (i) the light curve amplitude is the same in any of the photometric bands used and (ii) the light curve can be characterised by a simple sinusoidal variation. With these assumptions, each model light curve can be described by four parameters: light curve amplitude, period, phase-shift, and an offset from the photometric zero point. We allowed for a different zero-point offset for each measurement block (with data consisting of measurements of consecutive nights), even if the data were taken by the same instrument and filter combination due to the occasional year-long gaps between the measurement blocks. The best-fitting light curve period and amplitude is characterised by the minimum in the $C(P, \Delta m)$ function, obtained by the residual minimisation, where P and Δm are the period and amplitude of the light curve, respectively (see [Appendix A.5](#)).

The possible light curve periods were chosen in the range $P \in [1, 17]$ d. The upper limit was set to sufficiently cover the synchronised period (15.8 d), while the lower limit was set to 1 d as we used ‘nightly’ average values in many cases. We restricted our amplitude search range to $\Delta m \in [0, 0.2]$ mag (peak-to-peak, i.e. twice the sine amplitude), as the original $\Delta m \in [0, 0.6]$ mag range was found to be too wide and did not provide minima in the large amplitude domain. Our results are presented in [Fig. 1](#). While the $C(P, \Delta m)$ contour map shows several shallower minima, there is one main minimum, at $P = 16.2 \pm 0.5$ d, and $\Delta m = 0.027 \pm 0.005$, very close to the orbital period of Dysnomia (15.8 d). To check the robustness of this result, and obtain the period and amplitude uncertainties, we repeated the process by modifying the photometric data points by adding a random value with normal distribution using the specific measurement errors

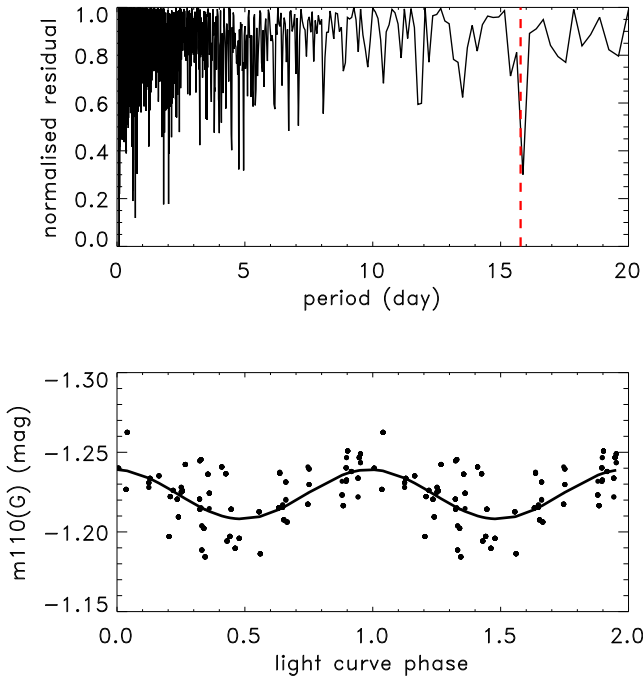


Fig. 2. Results of the *Gaia* light curve analysis. Upper panel: normalised residual spectrum of the Eris *Gaia* light curve. The red dashed line is at $P = 15.78$ d, the orbital period of Dysnomia; Lower panel: *Gaia* light curve folded with $f = 0.063 \text{ c d}^{-1}$. The solid curve is the best-fit sinusoidal, with a peak-to-peak amplitude of $\Delta m = 0.031 \pm 0.001$.

as standard deviations, and then repeating the fitting process several times for the whole data set.

2.3. *Gaia*

Gaia (Gaia Collaboration 2016, 2022) *G*-band photometry data of Eris (see Appendix A.4) was analysed using a residual minimisation algorithm to identify the possible frequencies in the light curve (see Fig. 2, upper panel). There is one strong minimum identified at the long period part of the residual spectrum at 15.87 ± 0.22 d (5.5σ), very close to the 15.78 d orbital period of Dysnomia. The *Gaia* light curve folded with this period (Fig. 2, bottom panel) was fitted with a sinusoidal curve using a Levenberg–Marquardt fitter which provided a peak-to-peak amplitude of $\Delta m = 0.031 \pm 0.001$ mag.

Both the ground-based data (Appendix A.3) and *Gaia* data strongly suggest that the light curve period of the Eris–Dysnomia system is equal to the orbital period of Dysnomia. As Dysnomia is significantly fainter than Eris in the visible range (1:0.0021, see Brown & Schaller 2007), a light curve variation of ~ 0.03 mag must be associated with Eris – and not with Dysnomia. The $P = 15.78$ d period rules out all shorter periods in the range between a few hours and a few days (see a detailed list in Sect. 1), as well as the semi-synchronised rotation period of $P = 14.56$ d obtained by Holler et al. (2020). However, we cannot exclude that the rotation period is not exactly the orbital period, but very close to it. In considering the ground-based and *Gaia* data, the latter demonstrates a smaller uncertainty in the period determination, providing an uncertainty of ~ 5 h. As we show below, the system must be extremely fine-tuned to exhibit an actual rotation period that is so close, but still different from the synchronised case when assuming a simple binary system. Therefore, we argue that the rotation of Eris and Dysnomia is

double-synchronised, namely, that the Eris–Dysnomia system is fully tidally locked.

As shown in Appendix A.2, Eris appears to have a considerable variability in the near-infrared $J - H$ colour, while all measurements show rather similar colours in the visible. One explanation for this behavior could be that the surface composition of Eris is not homogeneous and parts of the surface are covered with ices which have characteristic bands in the near-infrared, but have a reflectance similar to other materials in the visible (Fernández-Valenzuela et al. 2021). For instance, Eris is known to have strong methane features in its reflectance spectrum (Alvarez-Candal et al. 2020), especially between 1.5 and $1.8 \mu\text{m}$, close to the *H*-band. A variegation in surface composition may lead to a rotational variation in the near-infrared ($J - H$) colour, while leaving the visible range colours unchanged.

3. Possible tidal evolution scenarios

We used a simple tidal evolution model (see Appendix A.6) to find the possible initial conditions and physical characteristics of Eris and Dysnomia that could have led to the tidally locked rotation of Eris that is currently observed. Our main assumption is that the Eris–Dysnomia system was formed in a giant collision and begin tidal evolution from a much more compact configuration, and with Eris spinning significantly faster than today (Ragozzine & Brown 2009; Barr & Schwamb 2016; Arakawa et al. 2019). Each model configuration is set by the properties of Eris that are relevant for tidal interactions, namely, the tidal dissipation factor Q_p , the rigidity μ_p , and/or the second-order tidal Love number, k_{2p} ; and by the mass, M_s and effective radius R_s (or, equivalently the density ρ_s) of the satellite, Dysnomia. Previously Greenberg & Barnes (2008) studied the tidal evolution of the Eris–Dysnomia system, but they restricted their calculations to a specific Dysnomia radius of $R_s = 75$ km and mass of $M_s = 2.3 \times 10^{18}$ kg. In our model, we considered a wide range of R_s values that are compatible with the brightness constraints and that allow for radius and mass values as large as $R_s \approx 370$ km and $M_s \approx 5 \times 10^{20}$ kg (see Appendix A.6)

We first ran our code for a large set of models which covered a wide range of possible parameter values as shown in Fig. 3. For most of these cases, the final rotation periods of Eris, P_{pf} , remained below $P_{\text{pf}} \leq 1$ d, but there is a well-defined area in the $Q_p/k_{2p} - M_s$ plane where $P_{\text{pf}} > 1$ d, or, where synchronisation has been reached. This area is approximately defined by the two dashed lines in Fig. 3, which roughly satisfy a $Q_p M_s^2 / k_{2p} = \text{constant}$ relationship, as expected from the calculation of the spin rate change (Eq. (A.2)). As we are especially interested in those cases where the rotation of Eris has slowed down considerably, we selected starting parameters from the area defined above on the Q_p/k_{2p} vs. M_s plot (Fig. 3) to further map the parameter space in a second set of runs. The results of these runs are presented in Fig. A.7.

Even in our simple model, we have a rather wide range of parameters that lead to synchronised or nearly-synchronised rotation rates for Eris. However, there are some general conclusions that can be drawn from our simulations. First, it is feasible that a massive Dysnomia can considerably slow down the rotation of Eris, even forcing it to a synchronised rotation state. For instance, the rotation periods for Eris of $10 \text{ d} \leq P_{\text{pf}} \leq 15.78$ d can be reached for Dysnomia-to-Eris mass ratios of $10^{-2} \leq q \leq 3 \times 10^{-2}$. To reach such a large mass, Dysnomia has to be dark, with $p_{V_s} \leq 0.06$, in contrast to the very bright surface of Eris ($p_{V_p} = 0.96$). While it is possible to generate (near) synchronised rotation for $p_{V_s} \leq 0.06$, most of these runs require

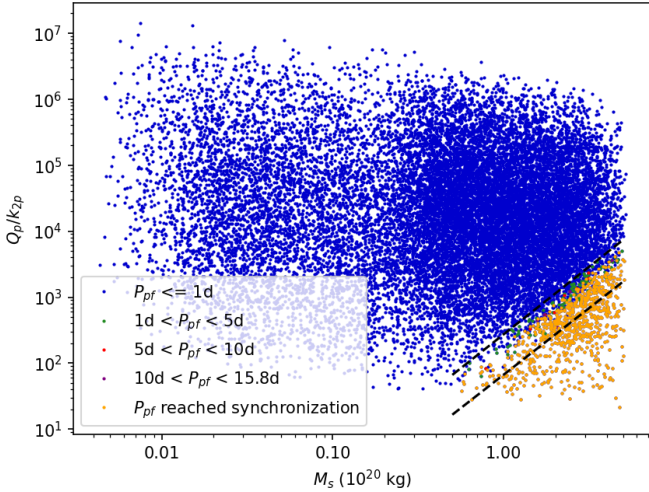


Fig. 3. Q_p/k_{2p} vs. the mass of Dysnomia M_s in the first trial runs. Orange symbols mark those cases which ended up in synchronised Eris rotation; blue symbols represent the cases with $P < 1$ d final Eris rotation periods. Dashed lines mark the region of M_s – Q_p/k_{2p} values that lead to a slowed-down rotation or tidal synchronisation of Eris (see text for details).

$p_{V_s} \lesssim 0.04$. Such a dark surface, and a correspondingly large size, is also suggested by the submm detection of Dysnomia with ALMA (Brown & Butler 2018), implying $R_s = 350 \pm 58$ km and $p_V = 0.04^{+0.02}_{-0.01}$.

Although our simulations were run for a wide range of material and tidal parameters assumed for Eris, mainly Q_p and μ_p , these parameters are canonically chosen in a much narrower range. In Fig. 4 we show a selection of those simulation runs for which the tidal quality parameter of Eris was $Q = 50, 100, \text{ or } 200$ ($\pm 10\%$) ($Q_p = 100$ is the canonical value usually assumed in the TNO tidal evolution calculations) and Eris’ rotation became tidally locked. For $Q_p = 100$ (red symbols in Fig. 4), synchronisation is reached for Dysnomia-to-Eris mass ratios of $q = 0.02$ – 0.03 , depending on the Eris rigidity parameter, μ_p , which can be in the range 4 – $20 \times 10^9 \text{ Nm}^{-2}$ for this Q_p value. These μ_p values correspond to the rigidity of ice ($\sim 4 \times 10^9 \text{ N m}^{-2}$), or a mixture of ‘ice and rock’, in the case of the higher μ_p values (c.f. Grundy et al. 2011). To obtain mass ratios of $q = 0.02$ – 0.03 Dysnomia has to be large ($D \gtrsim 600$ km) and its density has to be in the range $\rho_s = 1.8$ – 2.4 g cm^{-3} . These cases are also associated with very low, $p_V = 0.02$ – 0.03 , geometric albedos. In the case of a higher tidal quality parameter value (e.g., $Q_p = 200$), even higher mass ratios are required; and, correspondingly, the Dysnomia densities are also higher, $\rho_s \gtrsim 2.0 \text{ g cm}^{-3}$. In these cases, the allowed rigidity of Eris is $3 \times 10^9 \lesssim \mu_p \lesssim 8 \times 10^9 \text{ Nm}^{-2}$. A lower Q_p , however, would allow smaller Dysnomia masses from $q \approx 0.01$, with a significant dependence on the rigidity as higher q is required for higher rigidity values, up to $\mu_p = 3 \times 10^{10} \text{ Nm}^{-2}$. Due to the lower required mass, the density range allowed for Dysnomia is also wider, $\rho_s = 1.2$ – 2.4 g cm^{-3} . As indicated by the full range of simulations (see Fig. A.7) progressively smaller values of Q_p will allow for smaller Dysnomia mass values to be compatible with a synchronised Eris rotation. At $Q_p = 10$, our smallest value chosen, a Dysnomia with a mass ratio of $q \approx 0.006$ and density of $\rho_s \approx 1.0 \text{ g cm}^{-3}$ would be massive enough to lock the rotation of Eris. Precise absolute astrometry of the primary and secondary, which could be performed with ALMA (Brown & Butler 2019), may be able to detect the barycentric wobble and obtain the

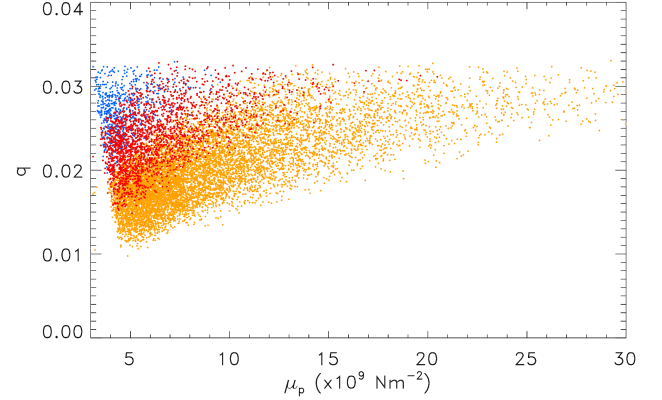


Fig. 4. Dysnomia-to-Eris mass ratio (q) vs. the rigidity of Eris (μ_p) in those simulation runs when Eris ended up in a synchronised rotation. The orange, red and blue colours mark Eris tidal parameters of $Q_p = 50, 100$ and 200 ($\pm 10\%$).

mass ratio, putting useful constraints on the tidal quality factor, Q_p .

4. Conclusions

In this Letter, we analyse long-term ground based photometric observations of Eris, complemented by measurements with the TESS and *Gaia* space telescopes. While the TESS data did not provide a conclusive rotation period, both the combined ground-based measurements and the *Gaia* data unambiguously point to a light curve period that is equal to the orbital period of Dysnomia, namely, a tidally locked rotation for Eris. The synchronised rotation of Eris, which is considered to be the consequence of a tidal interaction with Eris’ moon Dysnomia, puts constraints on the key physical properties of the satellite, as well as on those of Eris (as discussed in Appendix A.6). While the light curve or tidal evolution results do not directly constrain the shape, the very low spin rate of Eris indicates that its shape has to be very close to spherical, similarly to what has been observed for Pluto and Charon (Nimmo et al. 2017). In the case of Eris, both a homogeneous density interior model with a Maclaurin shape, or the Darwin–Radau model (see e.g., Murray & Dermott 2000) with a two-component, rocky core and an ice mantle interior, provide flattening values of $\epsilon \leq 0.0001$. This also means that the occultation shape and size solution (Sicardy et al. 2011) has to be very close to the spherical one, with $R = 1163 \pm 6$ km; this is an important constraint for thermal emission models, for instance. In addition, (Holler et al. 2021) suggested an oblate Eris as a possible cause behind the non-Keplerian orbit of Dysnomia; however, this now seems to be a less likely explanation.

Another proposal for explaining the non-Keplerian Dysnomia orbit assumes a centre of light-centre of body (CoL–CoB) offset that would be due to a large albedo pattern on the surface of Eris. Considering our best-fitting $\Delta m = 0.031$ mag amplitude, we investigated this scenario by assuming a single spot on the equator, coincident with the orbital plane of Dysnomia, and a viewing geometry as defined by the ‘combined’ solution in (Holler et al. 2021). In our simple model, the spot is visible in a fraction of the rotational phases and completely invisible in others; in these latter cases, Eris has a homogeneous, high-albedo surface. We varied the size of the spot with the spot albedo in a way that it always produces the required light curve amplitude, and we considered both Lommel–Seeliger and Lambert scattering laws. With this light curve amplitude, the maximum

CoL-CoB offset that could be obtained is ~ 40 km both for the Lommel–Seeliger and the Lambert scattering, and roughly similar values are obtained for the whole range of albedos considered. This is much smaller than the 462 km offset obtained by Holler et al. (2021). Considering the maximum possible size of ~ 600 km for Dysnomia, it is not feasible for the dominant part of the CoL-CoB offset to be due to features on the surface of the satellite; that is to say that the CoL-CoB offset is not a likely reason for the non-Keplerian orbit. The non-Keplerian orbit of Dysnomia could also be caused by a non-spherical shape of the satellite. A recent study of *Kepler/K2* light curves of trans-Neptunian objects (Kecskeméthy et al. 2022) shows that light curve amplitudes of TNOs remain larger at large ($D \geq 400$ km) sizes, where the asphericity of main belt asteroids drops significantly (Vernazza et al. 2021). While this could be due to an irregular-to-spherical transition at larger sizes for TNOs, their general low densities and high porosities disfavour this scenario. At the expected sizes of Dysnomia ($D \geq 600$ km), objects should be fairly round, even with higher densities and a considerable internal strength.

Assuming that the Eris–Dysnomia system formed in a giant impact, the rotation period of the post-impact Eris was probably much shorter, that is, on the order of a few hours. This fast rotation had to be slowed down by the tidal interaction with Dysnomia. As we show above, to reach synchronised rotation periods, Dysnomia has to be relatively massive (mass ratio of $q = 0.02$ – 0.03), assuming canonical values for the Q_p tidal dissipation factor and μ_p rigidity of Eris. This mass ratio is the second largest value in the trans-Neptunian region after the $\sim 8:1$ ratio in the Pluto–Charon system (see Barr & Schwamb 2016; Arakawa et al. 2019; Kiss et al. 2019, for earlier evaluations). We also note that currently the mass ratio in the Orcus–Vanth system is rather uncertain. The relatively high mass ratio is also associated with high Dysnomia densities of $\rho_s = 1.8$ – 2.4 g cm $^{-3}$, which are much greater than the typical densities of trans-Neptunian objects in this size range, $\rho = 0.5$ – 1.0 g cm $^{-3}$ (see e.g., Bierson & Nimmo 2019). In our tidal evolution model, unconventionally low Q_p tidal dissipation factors would allow for lower Dysnomia densities (down to $\rho_s \approx 1.2$ g cm $^{-3}$) and support the scenario of Eris reaching synchronised rotation at the same time. However, these values are still above the typical low densities of $R \approx 300$ km objects and would also require a low level of porosity. Collisional simulations have generally shown that intact moons with $10^{-3} \leq q \leq 10^{-1}$ could form in the trans-Neptunian region, assuming a wide range of impact parameters (Arakawa et al. 2019). More detailed impact and tidal evolution simulations should be able to identify the conditions leading to the present high-density Eris and high-density Dysnomia system.

Acknowledgements. The research leading to these results has received funding from the K-138962 grant of the National Research, Development and Innovation Office (NKFIH, Hungary). The data presented in this Letter were obtained from the Mikulski Archive for Space Telescopes (MAST). STScI is operated by the Association of Universities for Research in Astronomy, Inc., under NASA contract NAS5-26555. Support for MAST for non-HST data is provided by the NASA Office of Space Science via grant NNX09AF08G and by other grants and contracts. This research has made use of data and services provided by the International Astronomical Union’s Minor Planet Center. Part of the funding for GROND (both hardware as well as personnel) was generously granted from the Leibniz-Prize to Prof. G. Hasinger (DFG grant HA 1850/28-1). We are grateful to the CAHA and OSN staff. This research is partially based on observations collected at the Centro Astronómico Hispano Alemán (CAHA) at Calar Alto, operated jointly by Junta de Andalucía and Consejo Superior de Investigaciones Científicas (IAA-CSIC). This research was also partially based on observation carried out at the Observatorio de Sierra Nevada

(OSN) operated by Instituto de Astrofísica de Andalucía (CSIC). P.S.-S. acknowledges financial support by the Spanish grant AYA-RTI2018-098657-J-I00 “LEO-SBNAF” (MCIU/AEI/FEDER, UE). P.S.-S., J.L.O., N.M., and R.D. acknowledge financial support from the State Agency for Research of the Spanish MCIU through the “Center of Excellence Severo Ochoa” award for the Instituto de Astrofísica de Andalucía (SEV-2017-0709), they also acknowledge the financial support by the Spanish grants AYA-2017-84637-R and PID2020-112789GB-I00, and the Proyectos de Excelencia de la Junta de Andalucía 2012-FQM1776 and PY20-01309. We are also thankful to our reviewer for the useful comments. This work made use of Astropy: (<http://www.astropy.org>) a community-developed core Python package and an ecosystem of tools and resources for astronomy (Astropy Collaboration 2013, 2018, 2022). This work has made use of data from the European Space Agency (ESA) mission Gaia (<https://www.cosmos.esa.int/gaia>), processed by the Gaia Data Processing and Analysis Consortium (DPAC, <https://www.cosmos.esa.int/web/gaia/dpac/consortium>). Funding for the DPAC has been provided by national institutions, in particular the institutions participating in the Gaia Multilateral Agreement.

References

- Alvarez-Candal, A., Souza-Feliciano, A. C., Martins-Filho, W., Pinilla-Alonso, N., & Ortiz, J. L. 2020, *MNRAS*, 497, 5473
- Arakawa, S., Hyodo, R., & Genda, H. 2019, *Nat. Astron.*, 3, 802
- Astropy Collaboration (Robitaille, T. P., et al.) 2013, *A&A*, 558, A33
- Astropy Collaboration (Price-Whelan, A. M., et al.) 2018, *AJ*, 156, 123
- Astropy Collaboration (Price-Whelan, A. M., et al.) 2022, *ApJ*, 935, 167
- Barr, A. C., & Schwamb, M. E. 2016, *MNRAS*, 460, 1542
- Bierson, C. J., & Nimmo, F. 2019, *Icarus*, 326, 10
- Blanton, M. R., & Roweis, S. 2007, *AJ*, 133, 734
- Brown, M., & Butler, B. 2019, *Am. Astron. Soc. Meet. Abstr.*, 233, 354.12
- Brown, M. E., & Butler, B. J. 2018, *AJ*, 156, 164
- Brown, M. E., & Schaller, E. L. 2007, *Science*, 316, 1585
- Brown, M. E., Trujillo, C. A., & Rabinowitz, D. L. 2005, *ApJ*, 635, L97
- Brown, M. E., van Dam, M. A., Bouchez, A. H., et al. 2006, *ApJ*, 639, L43
- Canup, R. M. 2005, *Science*, 307, 546
- Carraro, G., Maris, M., Bertin, D., & Parisi, M. G. 2006, *A&A*, 460, L39
- Cutri, R., Skrutskie, M., Van Dyk, S., et al. 2003, *Explanatory supplement to the 2MASS all Sky Data release and Extended Mission Products*
- DeMeo, F. E., Fornasier, S., Barucci, M. A., et al. 2009, *A&A*, 493, 283
- Dobrovolskis, A. R., Peale, S. J., & Harris, A. W. 1997, in *Pluto and Charon*, eds. S. A. Stern, & D. J. Tholen (Arizona: University of Arizona Press), 159
- Duffard, R., Ortiz, J. L., Santos Sanz, P., et al. 2008, *A&A*, 479, 877
- Eisenstein, D. J., Weinberg, D. H., Agol, E., et al. 2011, *AJ*, 142, 72
- Fernández-Valenzuela, E., Pinilla-Alonso, N., Stansberry, J., et al. 2021, *Planet. Sci. J.*, 2, 10
- Fulchignoni, M., Belskaya, I., Barucci, M. A., de Sanctis, M. C., & Doressoundiram, A. 2008, in *The Solar System Beyond Neptune*, eds. M. A. Barucci, H. Boehnhardt, D. P. Cruikshank, A. Morbidelli, & R. Dotson (Arizona: University of Arizona Press), 181
- Gaia Collaboration (Prusti, T. et al.) 2016, *A&A*, 595, A1
- Gaia Collaboration (Valenari, A., et al.) 2022, *A&A*, in press, <https://doi.org/10.1051/0004-6361/202243940>
- Giorgini, J. D., Yeomans, D. K., Chamberlain, A. B., et al. 1996, *AAS/Division Planet. Sci. Meet. Abstr.*, 28, 25.04
- Goldreich, P., & Soter, S. 1966, *Icarus*, 5, 375
- Greenberg, R., & Barnes, R. 2008, *Icarus*, 194, 847
- Greiner, J., Bornemann, W., Clemens, C., et al. 2008, *PASP*, 120, 405
- Grundy, W. M., Noll, K. S., Nimmo, F., et al. 2011, *Icarus*, 213, 678
- Grundy, W. M., Noll, K. S., Buie, M. W., et al. 2019, *Icarus*, 334, 30
- Hastings, D. M., Ragozzine, D., Fabrycky, D. C., et al. 2016, *AJ*, 152, 195
- Holler, B. J., Benecchi, S., Mommert, M., & Bauer, J. 2020, *AAS/Division Planet. Sci. Meet. Abstr.*, 52, 307.06
- Holler, B. J., Grundy, W. M., Buie, M. W., & Noll, K. S. 2021, *Icarus*, 355
- Hromakina, T. A., Belskaya, I. N., Krugly, Y. N., et al. 2019, *A&A*, 625, A46
- Kecskeméthy, V., Kiss, C., Szakáts, R., et al. 2022, *ApJS*, accepted [arXiv:2210.06571]
- Kiss, C., Marton, G., Farkas-Takács, A., et al. 2017, *ApJ*, 838, L1
- Kiss, C., Marton, G., Parker, A. H., et al. 2019, *Icarus*, 334, 3
- Krühler, T., Küpcü Yoldaş, A., Greiner, J., et al. 2008, *ApJ*, 685, 376
- Lin, H. W., Wu, Y. L., & Ip, W. H. 2007, *AdSPR*, 40, 238
- Murray, C. D., & Dermott, S. F. 2000, *Solar System Dynamics* (Cambridge: Cambridge University Press)
- Nimmo, F., Umurhan, O., Lisse, C. M., et al. 2017, *Icarus*, 287, 12
- Ortiz, J. L., Gutiérrez, P. J., Sota, A., Casanova, V., & Teixeira, V. R. 2003, *A&A*, 409, L13
- Pál, A. 2012, *MNRAS*, 421, 1825
- Pál, A., Kiss, C., Müller, T. G., et al. 2016, *AJ*, 151, 117

- Pál, A., Szakáts, R., Kiss, C., et al. 2020, *ApJS*, 247, 26
- Perna, D., Barucci, M. A., Fornasier, S., et al. 2010, *A&A*, 510, A53
- Rabinowitz, D. L., & Owainati, Y. 2014, *AAS/Division Planet. Sci. Meet. Abstr.*, 46, 510.07
- Rabinowitz, D. L., Schaefer, B. E., & Tourtellotte, S. W. 2007, *AJ*, 133, 26
- Ragozzine, D., & Brown, M. E. 2009, *AJ*, 137, 4766
- Ricker, G. R., Winn, J. N., Vanderspek, R., et al. 2015, *J. Astron. Telesc. Instrum. Syst.*, 1, 014003
- Roe, H. G., Pike, R. E., & Brown, M. E. 2008, *Icarus*, 198, 459
- Sheppard, S. S. 2007, *AJ*, 134, 787
- Sicardy, B., Ortiz, J. L., Assafin, M., et al. 2011, *Nature*, 478, 493
- Skrutskie, M. F., Cutri, R. M., Stiening, R., et al. 2006, *AJ*, 131, 1163
- Smith, J. A., Tucker, D. L., Kent, S., et al. 2002, *AJ*, 123, 2121
- Snodgrass, C., Carry, B., Dumas, C., & Hainaut, O. 2010, *A&A*, 511, A72
- Tanga, P., Pauwels, T., Mignard, F., et al. 2022, *A&A*, in press, <https://doi.org/10.1051/0004-6361/202243796>
- Tegler, S. C., Romanishin, W., Consolmagno, G. J., & J., S., 2016, *AJ*, 152, 210
- Tody, D. 1993, in *Astronomical Data Analysis Software and Systems II*, eds. R. J. Hanisch, R. J. V. Brissenden, & J. Barnes, *ASP Conf. Ser.*, 52, 173
- Verbiscer, A. J., Helfenstein, P., Porter, S. B., et al. 2022, *Planet. Sci. J.*, 3, 95
- Vernazza, P., Ferrais, M., Jorda, L., et al. 2021, *A&A*, 654, A56

Appendix A: Supporting materials

A.1. Observations and data reduction

A.1.1. TESS data

The Transiting Exoplanet Survey Satellite (TESS, [Ricker et al. 2015](#)) observed Eris in Sector 30 with its Camera 1 and CCD 3 (Fig. A.1). The reduction of the TESS data was performed in the same way as described in [Pál et al. \(2020\)](#) which contains a detailed description of the reduction steps, photometry, and the derivation of the residual spectrum for frequency analysis. We only mention those steps here that are different from those in the [Pál et al. \(2020\)](#) pipeline. TESS photometry data of Eris are provided in Table A.1.

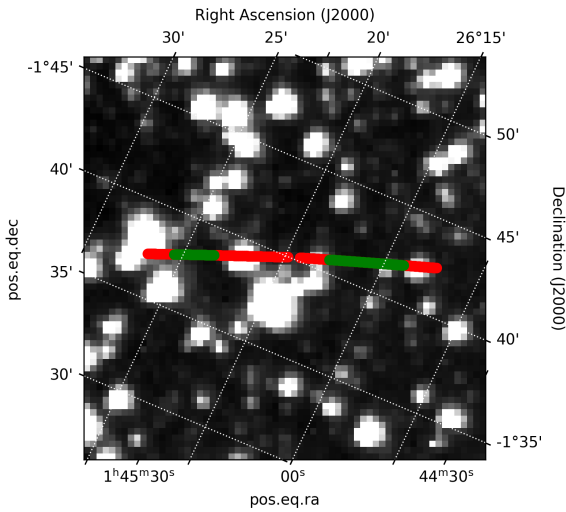


Fig. A.1. Eris’ path through the field-of-view of Sector 3, Camera 1, and CCD 3 of the TESS space telescope between Julian dates 2459115.89 and 2459142.52. The red and green parts mark those points that were excluded or considered for light curve analysis.

Table A.1. TESS photometry data of (136199) Eris (sample).

Julian Date	m (mag)	δm (mag)
2459119.81621	18.99754	0.46354
2459119.85788	18.65064	0.33787
2459119.89954	18.69310	0.31456
...

Note. We list the Julian date, brightness (m), and its uncertainty (δm) in the TESS photometric band. The table is available in its entirety at the CDS. All data points have 60 min integration time.

A significant portion of the light curve data had to be excluded due to Eris’ encounter with nearby background sources which left a dominant feature in the background-subtracted image. As shown in Fig. A.1, the two ‘green’ zones, where the vicinity of Eris was relatively clean, covers two blocks with lengths of 2.3 d and 6.6 d. In these blocks readout-to-readout variation of the background was estimated to be ~ 3 mag lower than the typical (~ 18.5 mag in the TESS bandpass) brightness of Eris, in the same measuring aperture. The residual spectrum obtained from the data of these two blocks merged is shown in Fig. A.2.

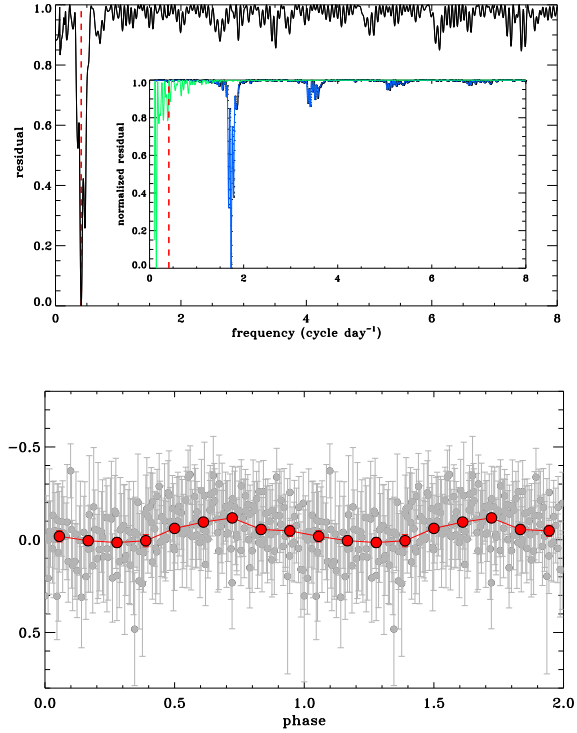


Fig. A.2. TESS light curve results. Top: Normalised residual spectrum of the TESS light curve of Eris. The insert shows the residual spectrum of the pixel-wise x- (blue) and y- (green) direction subpixel centroid positions. The most prominent characteristic frequency of $f = 0.411$ c/d is marked by a red vertical dashed line both in the main figure and the insert. Bottom: TESS light curve of Eris folded with $f = 0.411$ c/d. The red dots mark the binned light curve. These light curve data are presented in Table A.1) in an electronically readable format.

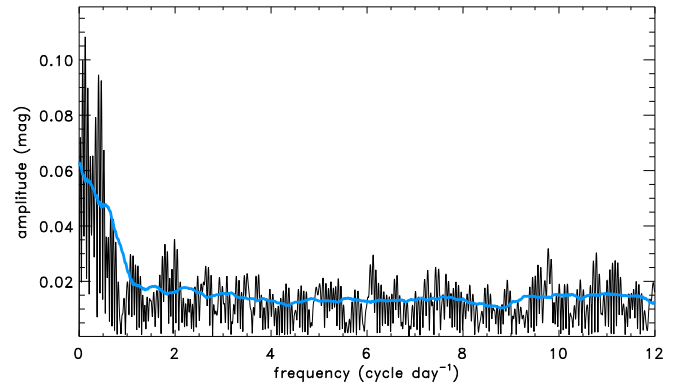


Fig. A.3. Fourier spectrum of the Eris TESS light curve. The blue curve is the rms amplitude, calculated using a running box and sigma clipping.

As TESS has large, ($21''$) pixels, the photometry of the source is affected by the relative position of the source inside the actual pixel and the projection of the total source flux into the neighbouring pixels. This is expected to introduce a periodic signal as the target moves through the field of view, and the characteristic frequency depends on the actual apparent speed of the target in the X and Y (pixel-wise) directions. To look for this effect, we checked the spectrum of the X and Y pixel fractions of centroid positions of Eris’ TESS photometry. The results are presented in the insert in Fig. A.2. These residual spectra show well defined minima at $f_x = 1.73$ c/d

(X-direction, blue curve in Fig. A.2) and $f_x = 0.14$ c/d (Y-direction, green curve). The residual spectrum of the TESS photometry data (main figure, black curve) shows a well-defined minimum at $f = 0.411 \pm 0.018$ c/d ($P = 58.394 \pm 2.571$ h). The uncertainty of the frequency is obtained as the FWHM of Gaussian fitted to the main frequency minimum in the residual spectrum. This frequency is different from the f_x and f_y frequencies identified above and could not be associated with any currently known instrumental effects. The light curve folded with this frequency is shown in Fig. A.2. The peak-to-peak amplitude of this folded light curve is $\Delta m = 0.132 \pm 0.037$ mag, obtaining the maximum-minus-minimum of the binned light curve as the amplitude and using standard error propagation in the calculation of the uncertainty.

We also derived the Fourier spectrum of the Eris TESS light curve (Fig. A.3, noting the factor of two conversion between the Fourier and peak-to-peak amplitudes). The rms Fourier amplitude (blue) curve shows that the 1σ noise is $\sigma_f \approx 0.015$ mag in the frequency range 1–12 c/d, and it increases considerably for lower frequencies, reaching ~ 0.065 mag at the lowest ones. These rms amplitudes can be used to estimate light curve detection upper limits (Δm_{lim}) for specific frequencies. Considering the detection limit as $3\sigma_f$, we obtain $\Delta m_{lim} = 0.045$ mag in the $f = 1\text{--}12$ c/d ($P = 2\text{--}24$ h) range, and $\Delta m_{lim} = 0.155$ mag at $f \approx 0.4$ c/d, namely, at the frequency where a prominent peak was identified in the residual spectrum, as discussed above. While a peak in the Fourier spectrum can be identified at the same frequency ($f = 0.411$ c/d) as in the residual spectrum, the signal-to-noise ratio is significantly lower here, $\sim 1.8\sigma$. Due to this limitation, we consider the $f = 0.411$ c/d ($P = 58.394$ h) peak as tentative. Also given the limited length of the TESS light curve blocks considered in the analysis (2.3 d and 6.6 d), it was not possible to detect light curve periods longer than ~ 3 d, and excluding the possibility to detect periods close to the orbital period (15.78 d). However, the Fourier spectrum shows that we can exclude rotation periods in the range of $P = 2\text{--}24$ h, which would be associated with peak-to-peak amplitudes of $\Delta m \geq 0.09$ mag, with a 3σ confidence; more specifically, if Eris had a rotation period in this range, it would have a very small amplitude that would likely be on the order of 0.03 mag or below.

A.2. GROND observations

Observations of Eris with the GROND instrument (Greiner et al. 2008) on the MPG 2.2m telescope at La Silla were made over three nights, with details given in Table A.3. Observations consisted of 8m4td observation blocks, that is, individual 120 s (115 s) exposures in JHK ($g'r'i'z'$) at each of the four telescope dither (td) positions, except for the first epoch with 2 s (20 s) exposures each at 2 td-positions. Since the Eris motion on the sky is below $0''.2/10$ min, the four different dither pointings were co-added. GROND data were reduced in the standard manner (Krühler et al. 2008) using pyraf/IRAF (Tody et al. 1993; Krühler et al. 2008). The optical imaging data ($g'r'i'z'$) was calibrated against the Sloan Digital Sky Survey (SDSS)¹ catalogue (Eisenstein et al. 2011) and the NIR data (JHK_s) against the 2MASS catalogue (Skrutskie et al. 2006). This results in typical absolute accuracies of ± 0.03 mag in $g'r'i'z'$ and ± 0.05 mag in JHK_s . Since the GROND dichroics were built after the Sloan filter system (Greiner et al. 2008), the colour terms are very small, below 0.01 mag, except for the i' band which is sub-

Table A.2. Ground-based photometry data of (136199) Eris (sample).

Telescope	Julian Date	m (mag)	δm (mag)	Filt.	t_{exp} (min)	t_{tot} (min)
GROND	2455436.91528	19.031	0.031	g'	8	8
GROND	2455438.69348	19.097	0.010	g'	8	8
GROND	2455438.75578	19.099	0.010	g'	8	8
...						
1.5m	2453647.53342	18.450	0.035	R	293.3	450.1
1.5m	2453648.55623	18.459	0.025	R	353.3	393.0
1.5m	2453649.56174	18.430	0.025	R	383.3	428.8
...						

Note. This table is available in its entirety at the CDS. The columns of the table are: Telescope name; mean Julian day of the measurement; target brightness (m) and its uncertainty (δm) in the respective filter band; filter; t_{exp} : sum of the individual exposure times used for this photometric point (as explained in the text); and t_{tot} : difference between the end of the last and the start of the first measurement used to obtain this specific photometric point.

stantially narrower than the SDSS i' band: $i'_{SDSS} - i'_{GROND} = (-0.023 \pm 0.010) + (0.216 \pm 0.054) \cdot (i'_{SDSS} - z'_{SDSS})^2$. In order to minimize the impact of variability in the comparison stars, relative photometry was done against the same observation (2010-08-31T08:51-09:03). Since Eris moved by about $1'$ over the 3-day observing period, care was taken to select comparison stars such that they were covered in all observations. GROND photometry data are listed in Table A.2. The GROND J and H colours in Table A.2 and the J-H colour index in Table A.5 are given in the AB photometric system. To convert them to the Vega system, we used the following conversions: $J_{Vega} = J_{AB} - 0.91$ and $H_{Vega} = H_{AB} - 1.38$ from (Blanton & Roweis 2007).

We compared the colours from our GROND photometry with values from the literature, as shown in Table A.5. We converted the GROND g,r,i,z colours to Johnson/Cousins BVRI, as described in Smith et al. (2002). Near-infrared colours were converted from the respective systems used in the specific papers to a common 2MASS system, as described in the table caption. The colours from the new GROND measurements are in a relatively good agreement with the values from other studies in the visible bands. However, in the near-infrared, the J-H colours show large variations. The J-H values range from -0.290 ± 0.045 to 0.287 ± 0.114 , that is, a ~ 0.58 mag difference between the lowest and highest colour values.

A.3. Other ground-based observations

We obtained ground-based photometry data for Eris from four telescopes (see Table A.3). All the data were reduced using standard calibration steps with the FITSH (Pál 2012) software package, namely: bias, dark, and flat corrections were applied. We then we performed aperture photometry on Eris and on selected comparison stars. Using the comparison stars as the standard stars in our sample, we obtained magnitudes from the Pan-STARRS DR2 catalogue and used these magnitudes to do an approximate standard calibration of Eris via a simple linear fitting of the observed and the catalogue magnitudes. In most cases, only one filter was used, so a more sophisticated standard calibration was not possible. When required, the Pan-STARRS magnitudes were converted to Johnsons R magnitude based on the

¹ <http://www.sdss.org>

² <https://www.mpe.mpg.de/~jcg/GROND/calibration.html>

Table A.3. Summary table of ground-based observations.

Telescope	Instrument	Date range	Number of nights	Filter	Reference
TESS	Camera 1	2020.09.27.-2020.10.16.	19	TESS Bandpass	(Ricker et al. 2015)
MPG 2.2m	GROND	2010.08.28.-2010.08.31.	3	$g'r'i'z'$ JH*	(Greiner et al. 2008)
1.5m	Roper, Andor	2005.10.03.-2020.10.16.	18	Johnson R, Clear	(https://www.osn.iaa.csic.es/en/page/15-m-telescope)
CA2.2	CAFOS2.2	2007.01.11.-2007.01.16.	6	Johnson R	(http://www.caha.es/CAHA/Instruments/CAFOS/)
La Hita	SBIG STX-16803-3	2014.10.24.-2014.10.28.	5	Clear	(https://fundacionastrohita.org/instrumental/)

Note. We are listing here the telescope, instrument (camera), date range, number of nights, and the filters used. *:GROND JH magnitudes are in the AB system. These observations, taken between JD = 2453647.53342 and 2459139.5323, covered heliocentric and observer distances of $r_h = 95.9$ -96.9 au, $\Delta = 95.0$ -96.6 au, and phase angles $\alpha = 0.12$ -0.58 deg.

method described in Smith et al. (2002). Typical observations consisted of a few individual integrations per night, covering an interval of a few hours. As our aim with these measurements was to look for long-term variations, we produced an average 'per-night' photometric point from the individual integrations. These have considerably improved the signal-to-noise ratio (S/N) values as well. These 'per-night' photometry data are presented in Table A.2.

Data obtained with a specific telescope or instrument have been divided into measurement blocks, each typically containing data obtained over a few consecutive nights and are separated from the other blocks by a longer period (up to a year). To avoid problems with absolute calibration we allowed a different absolute brightness zero point offset for each of these blocks in the subsequent light curve analysis. Due to the slow apparent motion of Eris heliocentric and observer distance, and phase angle corrections were applied only in those cases when the measurements covered a longer period – this was the case for some of the literature data (e.g. Rabinowitz et al. 2007) but not for our own measurements, however, as they have a typical measurement block length of a few days. In the case of the GROND and Rabinowitz et al. (2007) data, the observations were performed by alternating between the $g'-r'$ and the $V-B$ filters. For our light curve period search, we converted the g' data to the r' band using a mean $g' - r'$ colour, and the B data to V data using a mean $B - V$ colour to increase the number of data points for these measurement sequences. Assuming that the spin pole of Eris is coincident with the orbital pole of Dysnomia, and using the pole solution from (Holler et al. 2021), we estimated that the aspect angle of Eris' pole changes between $\vartheta \approx 129$ -133 deg, that is, $\Delta\vartheta \approx 4$ deg between the first and last date of the ground-based measurement sequence (see Table A.3). As the aspect angle is not at its extremes, this does not affect the light curve amplitudes or the detectability of the light curves through different data sets in any particular way.

A.4. Gaia data

The Eris Gaia data is available in the third Gaia Data Release (Gaia Collaboration 2022), accessible in the Gaia Science Archive³ through the `gaiadr3.sso_observation` table. The table contains data obtained during the transit of the source on a single CCD, during a single transit. More details about the SSOs in the Gaia DR3 are discussed in Tanga et al. (2022).

Gaia G-band data of Eris was corrected for heliocentric and observer distance and phase angle, using spacecraft-centric data obtained from the NASA Horizons system (Giorgini et al. 1996). We applied a linear phase angle correction using the heliocentric and observer distance-corrected brightness values. We used

³ <https://gea.esac.esa.int/archive/>

Table A.4. Gaia photometry data of (136199) Eris

Julian Date	m (mag)	δm (mag)
2456900.12065	-1.21999	0.01012
2456900.12071	-1.21999	0.01012
2456900.12076	-1.23254	0.01313
...

Note. This table lists the Julian date, brightness (m), and its uncertainty (δm) in the TESS photometric band. Brightness has been corrected for heliocentric and observer distance, and phase angle. The full table is available at the CDS.

these reduced magnitudes (provided in Table A.4) for the period search.

A.5. Period finding method

We used a residual minimisation method to find the best-fitting light curve period and amplitude in our long-term ground-based photometry data (Sect. A.3). We chose an amplitude of Δm and period P , and determined the best fitting light curve phase using a Levenberg–Marquardt minimisation algorithm. With these best-fit phase models, we calculated the following $C(P, \Delta m)$ value for each P - Δm pair:

$$C(P, \Delta m) = \sum_i \frac{w_i}{N_i} \sum_j \left(\frac{m_{ij}^{mod} - m_{ij}^{obs}}{\delta m_{ij}} \right)^2, \quad (\text{A.1})$$

where the index j denotes the individual, night-averaged values, and i denotes the measurement blocks; m_{ij}^{obs} and m_{ij}^{mod} are the measured and model photometry values, respectively, δm is the photometric uncertainty, while N_i is the number of individual data points in the measurement block; w_i are the weights of the individual measurements blocks which have been chosen to be $\sqrt{N_i}$. We expect that the best-fitting period-amplitude values provide the lowest $C(P, \Delta m)$ values. We searched the period range $P \in [1\text{d}, 17\text{d}]$, where the upper limit is set to cover the 15.8 d is the orbital period of Dysnomia (and it would correspond to a synchronised rotation). The 1 d lower limit has to be set due to the 'per night' photometry points used in the case of most ground-based measurements.

To check the efficiency of our period and amplitude finding method, we generated a synthetic sinusoidal light curve with a peak-to-peak amplitude of $A = 0.040$ mag. We sampled this light curve exactly at the same dates as our real data and divided these photometry points into the same blocks as the original ones, as described in Sect. A.3. We used the mean photometry error in each measurement block, as assigned a photometric uncertainty to each photometry point in this specific block by assuming a

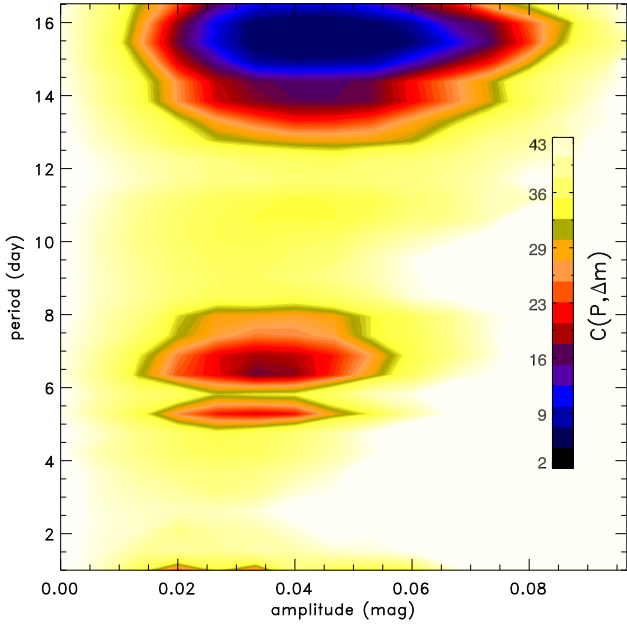


Fig. A.4. $C(P, \Delta m)$ map obtained with the period-amplitude finding algorithm using a synthetic signal with $P = 15.78$ d (the orbital period of Dysnomia), as described in detail in the main text.

random value with a normal distribution with a standard deviation equal to the mean error. We generated a large sample of synthetic light curves using random light curve phases and different random error assignments, and we ran our period and amplitude finding residual minimalisation method. The results show that the period and amplitude can be well recovered with our method, and the expected uncertainty is $\delta P \approx 0.5$ d in the period and $\delta m \approx 0.005$ mag in the light curve amplitude. An example of these χ^2 results is shown in Fig. A.4.

While the true period and amplitude of the original signal is correctly identified within the uncertainties (dark blue region in Fig. A.4), there are other, shallower minima popping up at various frequencies, caused by aliasing. For instance, one of these periods is at $P = 1$ d due to the single, combined photometry points per night in the case of a number of measurement blocks. The match of measurements with the best-fit light curve obtained by the residual minimalisation method is shown in Fig. A.5 for several measurement blocks.

A.6. Tidal evolution model

The satellites of the largest Kuiper belt objects are thought to be formed by large collisions (Barr & Schwamb 2016) and, remarkably, all large Kuiper belt objects with diameters $D \geq 1000$ km have confirmed satellites (Kiss et al. 2017). The tidal evolution of these systems depends on the size, mass, formation distance, and material properties of the bodies. Tidal evolution has certainly led into a double-synchronous state in the case of the Pluto-Charon system (Dobrovolskis et al. 1997), but in the Haumea system even the larger satellite Hi'iaka could not reach synchronous rotation (Hastings et al. 2016). Although the spin period of Eris seems to be rather well defined now by this present work, it is an interesting question whether the possible rotation periods of Eris – ranging from a few hours to the orbit-synchronous state – are feasible in terms of tidal evolution, using the current knowledge on the system components. This is especially interesting after the likely detection of Dysnomia in the

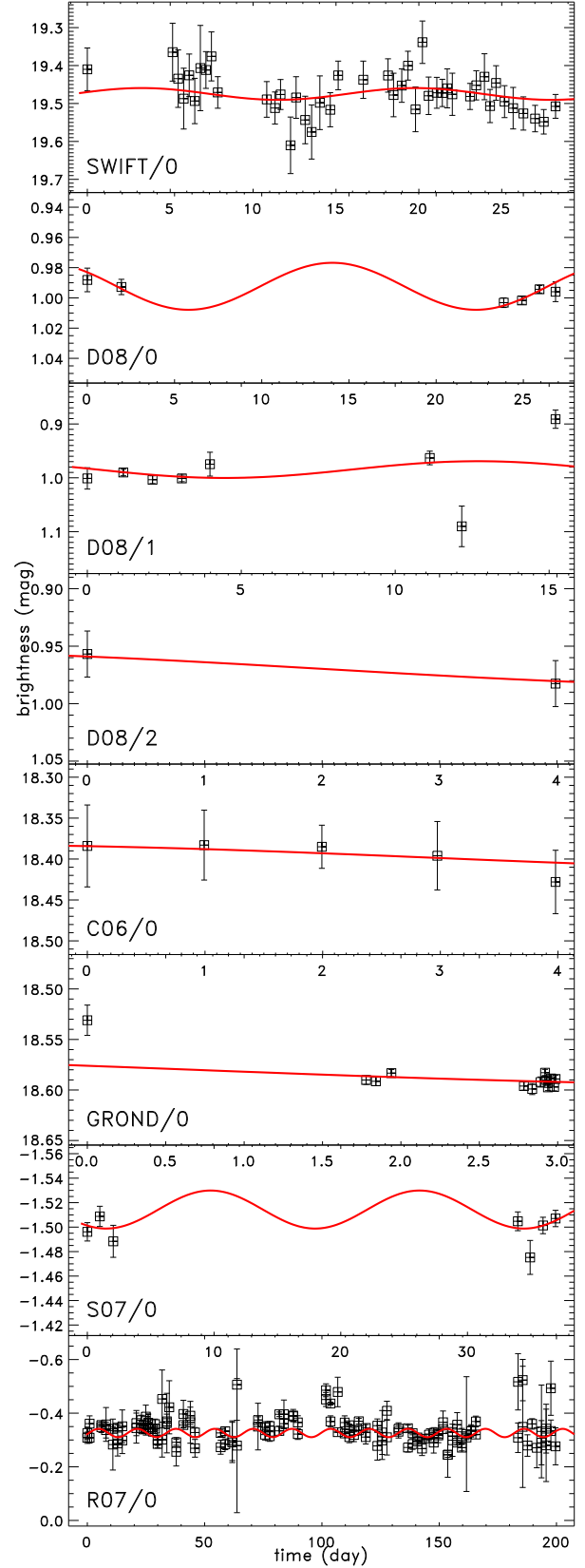


Fig. A.5. Best-matching sine functions (red curve, 15.78 d, i.e. the orbital period of Dysnomia) fitted to the long term photometry data of Eris for some of the telescopes considered in our analysis. Time is defined with respect to the start of the measurement block and brightness is in the actual apparent or reduced system, depending on the telescope and measurement block, as marked in the bottom left corners and described in the text.

Table A.5. Colours derived from GROND photometry.

SDSS photometry	g-r (mag)	g-i (mag)	r-i (mag)	g-z (mag)	J-H (mag)
this work	0.499±0.004	0.623±0.006	0.124±0.004	0.594 ± 0.013	-0.479±0.089
Johnson/Cousins photometry	B-V (mag)	V-R (mag)	R-I (mag)	R-J (mag)	J-H (mag)
this work	0.709±0.040	0.358±0.030	0.359±0.02	0.64±0.04	0.024 ±0.028
Carraro et al. (2006)	0.823±0.023	0.391±0.023	0.386±0.012	-	-
Fulchignoni et al. (2008)	0.71±0.02	0.45±0.02	0.33±0.03***	-	-0.29±0.045*
DeMeo et al. (2009)	-	-	-	-	0.054±0.070****
Perna et al. (2010)	-	-	-	-	0.022±.070****
Snodgrass et al. (2010)	0.78±0.01	0.45±0.03	0.33±0.02	0.52±0.02	0.287±0.114**
Tegler et al. (2016)	0.75±0.02	0.43±0.02	-	-	-
Alvarez-Candal et al. (2020)	0.782±0.003	0.393±0.003	-	-	-
Fernández-Valenzuela et al. (2021)	0.74±0.06	0.39±0.05	0.38±0.08***	-	-
Verbiscer et al. (2022)	0.805±0.015	0.389±0.049	-	-	-

Note. First row shows the colours directly derived from GROND photometry using the g, r, i, z, J, and H bands in this work. We note that the J, H magnitudes are in the AB system. The second row lists the colours transformed to the B, V, R, I, J, H bands, as described in Smith et al. (2002) and Blanton & Roweis (2007). The additional rows represent the values obtained earlier in other studies. *: From (Brown et al. 2005) **: Snodgrass et al. (2010) converted to J-H from $J - H_s$ ***: Calculated from V-R and V-I, ****: converted from UKIRT JH to 2MASS JH, using (Cutri et al. 2003)

ALMA 870 μm data, which suggests that Dysnomia could be a massive satellite with a diameter of ~ 700 km (Brown & Butler 2018).

We used the simple tidal evolution model from (Murray & Dermott 2000), also used by Hastings et al. (2016), to calculate the evolution of the satellite orbit (only the semi-major axis in this approximation) and the spin evolution of Eris and Dysnomia. In this model the satellite orbit and the equator of Eris are assumed to be co-planar. Some of the main characteristics of the system originate from the orbit of Dysnomia (Holler et al. 2021), as it defines the current semi-major axis of the satellite orbit, a_f , the orbital period, P_{orb} , and the system mass, M_{sys} . Eris is expected to be nearly spherical and the radius and V-band geometric albedo of Eris, $R_p = 1163 \pm 6$ km and $p_{Vs} = 0.96$ are quite precisely known from a stellar occultation (Sicardy et al. 2011). The rate of change of the spin frequency depends on the ratio of the second-order tidal Love number and the tidal quality factor, k_{2p}/Q_p , the mass and size of Eris, M_p and R_p , the actual semi major axis of the satellite orbit, a , and the mass of Dysnomia, M_s :

$$\dot{\omega}_p = -\text{sign}(\omega_p - n) \frac{15}{4} \frac{k_{2p}}{Q_p} \frac{M_s^2}{M_p} \left(\frac{R_p}{a}\right)^3 \frac{G}{a^3}. \quad (\text{A.2})$$

The Q_p tidal quality factor was chosen to be in the range of 10–1000 (Goldreich & Soter 1966; Murray & Dermott 2000), allowing for a variation of one order of magnitude around the canonical $Q = 100$. The second-order tidal Love number k_2 is calculated from the rigidity μ following Hastings et al. (2016). The μ_p rigidity of Eris was also allowed to vary in a wide range from 10^9 to 10^{11} N m^{-2} , which should be sufficiently wide to cover the typical values from icy to rocky interiors (Murray & Dermott 2000).

The evolution of the semimajor axis can be expressed by the equation below, following (Hastings et al. 2016):

$$a(t) = (a_f - a_0)(t/T)^{2/13} + a_0, \quad (\text{A.3})$$

where T is the age of the Solar System, a_0 is the initial semi-major axis, and a_f is the present semimajor axis.

The brightness ratio of Eris to Dysnomia in the F606W band of the HST is 0.0021 (Brown & Schaller 2007), which defines the size of Dysnomia, R_s , for a specific Dysnomia geometric albedo chosen. Among trans-Neptunian objects and satellites, a very wide range of albedos are possible from extremely dark surfaces to very bright ones. While Dysnomia is probably large and dark (Brown & Butler 2018), we chose a geometric albedo in the range of $p_{Vs} = 0.02$ – 0.8 for Dysnomia for our model calculations. Trans-Neptunian objects with diameters below ~ 500 km are expected to have a high porosity and low bulk density (Grundy et al. 2019). As a reasonable range, we first assumed $\rho_s = 0.5$ – 2.4 g cm^{-3} , which (together with R_s obtained above) defines the mass of Dysnomia, M_s . The lower limit is the typical density of objects in the few hundred km size in the Kuiper belt (see e.g. Grundy et al. 2019). The upper limit in density of 2.4 g cm^{-3} is the bulk density of Eris, and, in extreme cases, Dysnomia might have a similar density (as argued e.g. in Holler et al. 2021). The mass of Eris is obtained as $M_p = M_{sys} - M_s$, and we use the mass ratio, $q = M_s/M_p$, to characterise the system in this sense.

In addition to the system parameters described above, following (Canup 2005), the initial semi-major axis of the satellite orbit is assumed to be $a_s = 1.2 \cdot a_R$, and $a_R = 2.456 \cdot R_p \cdot (\rho_p/\rho_s)^{1/3}$ is the Roche limit. The initial spin period of Eris is set by the breakup limit $-\omega_c = (GM_p/R_p^3)^{1/2} = (4\pi G \rho_p/3)^{1/2}$ – and we allowed spin periods of $[1-2] \cdot \omega_c$.

We ran the tidal evolution model for a large number of cases assuming independent, random values of k_{2p} , Q_p , ρ_s , and p_{Vs} chosen in the intervals described above. We also assume that once Eris has reached synchronous rotation in a simulation run, it remains in this state and the rotation period just changes with the changing semi-major axis and orbital period.

In Fig. A.6, we demonstrate the sensitivity of the model to the Q_p tidal parameter. The model runs presented in this figure have led to very different final Eris rotation periods from $P_{pf} \approx 1$ d to synchronised rotation when all starting parameters were kept the same, except Q_p , which was varied across the range $13.5 \leq Q_p \leq 17.5$. A very similar sensitivity is seen for the

k_{2p} parameter (see Eq. A.2), however, this parameters is calculated from the μ or μ_{eff} values.

We also present in Fig. A.7 scatter plots of those key parameter combinations (mass ratio of q , k_{2p} , and Q_p as the tidal parameters, μ_p as the rigidity, and ω_0 as the starting angular speed of Eris, density of ρ_s , albedo of p_{vs} , and radius, R_s , of Dysnomia) for which our tidal evolution model resulted in $P_{pf} > 1$ d final rotation periods for Eris. The different colours correspond either to ranges of different P_{pf} values or a final synchronised state.

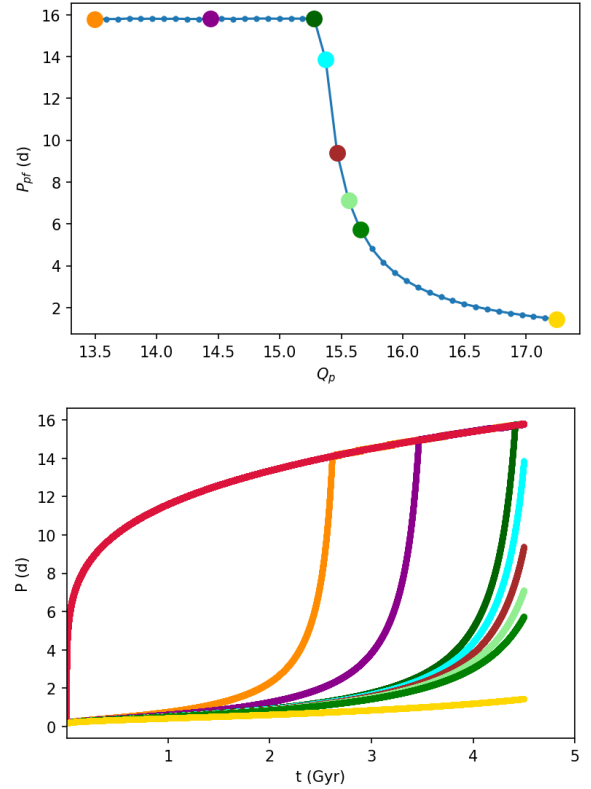


Fig. A.6. Demonstration of the sensitivity of the model to the Q_p parameter. Top panel: The final rotation period vs. Q_p parameter. Each dot in this plot corresponds to the Q_p and the final Eris rotation period, P_{pf} , of a specific run. All other model parameters were kept the same. Bottom panel: Evolution of the rotation period of Eris, using the models presented in the upper panel. The colours of the curves correspond to the colour of the symbols on the upper panel, the red curve is the evolution of the orbital period.

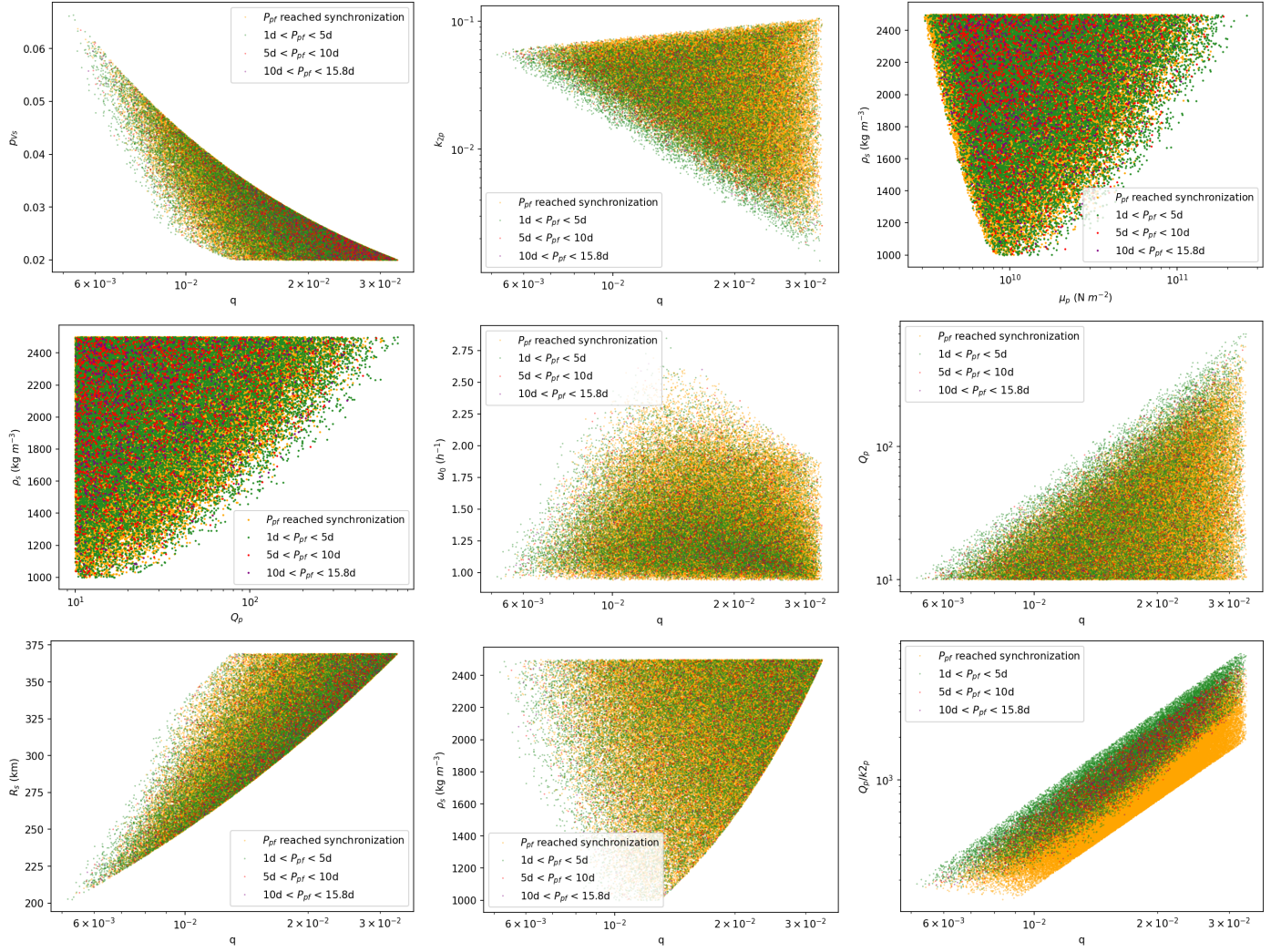


Fig. A.7. Scatter plots of model parameters for the selected Q_p – M_s range cases. The colours correspond to ranges of the final rotation period of Eris (P_{pf}), as indicated in the legend boxes.